multi-dimensional case with more complicated atomic arrangements.

References

BAK, P. (1986). *Phys. Rev. Lett.* **56**, 861–864.
GERMAIN, G., MAIN, P. & WOOLFSON, M. M. (1970). *Acta Cryst.* B**26**, 274–285.
GERMAIN, G., MAIN, P. & WOOLFSON, M. M. (1971). *Acta Cryst.* A**27**, 368–376.
HAO QUAN, LIU YI-WEI & FAN HAI-FU (1987). *Acta Cryst.* A**43**, 820–824.
JANSSEN, T. (1986). *Acta Cryst.* A**42**, 261–271.
LI FANG-HUA, WANG LI-CHEN & FAN HAI-FU (1987). *Mater. Sci. Forum*, **22–24**, 397–408.
SHECHTMAN, D., BLECH, I., GRATIAS, D. & CAHN, J. W. (1984). *Phys. Rev. Lett.* **53**, 1951–1953.
WOOLFSON, M. M. (1987). *Acta Cryst.* A**43**, 593–612.

Acta Cryst. (1990). A**46**, 478–485

A Synchrotron X-ray Study of the Surface Layer in Stoichiometric $LiNbO_3$ on Modulation by an Applied Electric Field*

BY KENNY STÅHL

Inorganic Chemistry 2, *University of Lund, PO Box* 124, *S*-221 00 *Lund, Sweden*

ÅKE KVICK†

Chemistry Department, Brookhaven National Laboratory, Upton, New York 11973, *USA*

AND S. C. ABRAHAMS

AT&T Bell Laboratories, Murray Hill, New Jersey 07974, *USA and Institut für Kristallographie der Universität Tübingen, Charlottenstrasse* 33, *D*-7400 *Tübingen, Federal Republic of Germany*

(*Received* 24 *April* 1989; *accepted* 16 *January* 1990)

Abstract

A single crystal of stoichiometric lithium niobate has been studied, using high-resolution synchrotron X-rays, under an electric field applied along the polar crystallographic *c* direction. A crystalline plate, 0·2 mm thick along the *c* direction, was polarized by a ±900 V square wave of frequency 50 and 230 Hz. Electronic gating ensured that the scattered intensities were recorded only during the central 50% of the square-wave duration. The results show that the stoichiometric crystals have surface layers under the Al electrodes that differ in the *c* cell dimension from the bulk by about $\Delta c/c = 6\times10^{-4}$. The resulting *c* lattice vector is close in length to that of congruent $Li_{0\cdot941}Nb_{1\cdot012}O_3$, although the composition of the surface layer may only be inferred; modification by Al in-diffusion may also be possible. The surface-layer thickness is estimated to be of the order of 0·01 mm.

* This research was carried out at Brookhaven National Laboratory under contract DE-AC02-76CH00016 with the US Department of Energy and supported by its Division of Chemical Sciences, Office of Basic Energy Sciences.

† Present address: European Synchrotron Radiation Facility, BP 220, F-38043 Grenoble CEDEX, France.

0108-7673/90/060478-08$03.00

Introduction

Lithium niobate is a readily grown high-quality single-crystal material widely used in many electronic and electro-optic devices. A detailed review of the chemisty and physics of lithium niobate has been given by Räuber (1978) and, more recently, in *Properties of Lithium Niobate* (EMIS, 1989). A detailed study of both the congruent and stoichiometric crystal structure has been presented by Abrahams & Marsh (1986).

Lithium niobate has a congruent melting point at 1513 K corresponding to the chemical composition $Li_{0\cdot946}NbO_{2\cdot973}$ (Carruthers, Peterson, Grasso & Bridenbaugh, 1971), as found in single crystals grown from the melt. It is however possible to form stoichiometric crystals by lithium vapor-phase equilibration of congruent material for about 800 h at 1373 K (O'Bryan, Holmes & Kim, 1984). The physical properties of lithium niobate are strongly dependent on composition; for instance, the congruent phase has a ferroelectric Curie temperature T_c = 1402 K, whereas the stoichiometric phase has the considerably higher T_c of 1471 (2) K (Gallagher & O'Bryan, 1985).

The effect of various kinds of field-induced atomic displacements on structure (*e.g.* electric, elastic, magnetic and thermal) has been of interest for many years (Compton & Allison, 1949, and early references therein; Abrahams, 1979). Most studies of these effects have been concerned with results in equilibrium, *i.e.* following the application and withdrawal of the field. Early X-ray diffraction experiments on dielectric crystals under the application of DC fields resulted in irreproducible effects, due largely to the slow decay of space charges produced within the crystalline sample by the field. It became apparent that the experimental method should make use of fields, preferably with square waveform, and a detection system that is precisely and appropriately gated to the applied waveform.

The development of such a system has led to a series of studies on the effect of an electric field applied to lithium niobate, using high-resolution synchrotron X-rays as the probe. The present paper discusses the change in surface properties of a stoichiometric single crystal of $LiNbO_3$ under the application of an electric field. During the study of this material, distinctly split Bragg diffraction profiles were observed that were not present under identical experimental conditions for congruent crystals. A comparison of peak profiles from a congruent and a stoichiometric crystal is shown in Fig. 1. An analysis of the observations for the stoichiometric compound is given below. The splitting is attributed to the formation of a new layer on the outer surfaces of the crystal plate. The surface layers are concentrated in the areas below the Al electrodes.

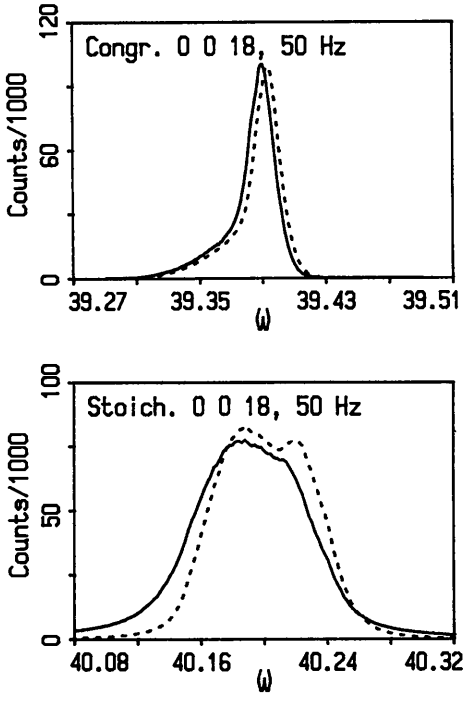

Fig. 1. A comparison of 00.18 peak profiles from crystals of congruent and stoichiometric $LiNbO_3$.

Experimental

A single-crystal plate with dimensions $10\times10\times0{\cdot}2$ mm was cut and polished from a large boule of Czochralski-grown crystal and then converted to stoichiometric composition by lithium vapor-phase equilibration. The polished {00.1} crystal faces were prepared for electroding by etching in a fluorine plasma. A layer of Al about 1000 Å thick was evaporated on each face, leaving a window frame of material 0·5 mm wide around the edge of the face without electrode material to prevent the possibility of edge effects under the application of an electric field. Electrical leads were connected to the Al layers by thin silver epoxy. The electrodes were connected to a power supply producing ±900 V square waves. Pulses associated with the middle 50% of the positive- and negative-going parts of the square wave were used to gate the NaI scintillation detector output to two different counting scalers. The square-wave voltage was applied at 50 or 230 Hz during the experiments to prevent the build up of compensating field charges at the electrode interfaces. The voltage across the crystal produced by the square wave is generated according to the formula

$$V = V_0[1-\exp(-t/RC)]. \qquad (1)$$

Integration over the central portion of the wave yields an effective average voltage of

$$V = V_0(1+4(f/f_c)\{\exp[-\tfrac{3}{8}(f_c/f)] - \exp[-\tfrac{1}{8}(f_c/f)]\}), \qquad (2)$$

where f is the frequency and f_c is the inverse of the RC time constant. The time constant in this experiment was measured as 2 ms, giving a 10% voltage reduction at 50 Hz and a 60% reduction at 230 Hz.

The experimental arrangement is illustrated in Fig. 2. The crystal polarity sense was determined from the pyroelectric response as measured with a current amplifier. The crystallographic (00.1) face was found to become positively charged upon cooling.

The X-ray data were collected at the National Synchrotron Light Source Crystallography Station X-7B on a Huber six-circle diffractometer with detector motion in the vertical plane, using NaI scintillation detectors (Kvick, 1989). The $\lambda = 0{\cdot}989$ Å X-ray beam was obtained by monochromatization of the bending-magnet radiation with an Si(111) double crystal followed by focusing in the horizontal direction with an Rh-coated mirror at a grazing angle of 3 mrad. The synchrotron ring current during the experiment was in the range 45 to 145 mA and the detected scattered signal was attenuated by Pb foils placed in front of the scintillation counter to ensure a linear response.

The primary beam was collimated so that the 'foot print' of the beam, even at the highest Bragg angles, did not extend outside the Al-coated areas. The electrodes were arranged to ensure that no obstruction of primary or reflection beams occurred.

Two profiles for each reflection were collected synchronously in an ω step-scan mode with an ω-step width of 0·002°. The intensity for each step was collected for a preset number of counts obtained from a thin Kapton film, inserted in the primary beam after the final exit collimation, and monitored with a scintillation detector. The recorded profiles are given in Fig. 3. Reference profiles before the field was applied and from areas outside the electrodes are also shown in Fig. 3.

Data analysis

The diffraction profiles were analyzed by least-squares fit to the recorded profiles, assuming components from two different Gaussian peak profiles, using the expression

$$I(\omega) = [I_n/\sigma_n(2\pi)^{0\cdot5}] \exp(-x_n^2/2\sigma_n^2) + [I_s/\sigma_s(2\pi)^{0\cdot5}] \exp(-x_s^2/2\sigma_s^2) + I_{bgr}, \quad (3)$$

where $x_n = \omega_n - \omega_0 + 0\cdot5\Delta\omega$, $x_s = \omega_s - \omega_0 - 0\cdot5\Delta\omega$ and $\Delta\omega$ is the splitting between the two peaks. The subscripts s and n denote stoichiometric and new phases, respectively. The parameters refined were the observed integrated intensities I_n and I_s, the Gaussian width parameters σ_s and σ_n, the observed shifts ω_s and ω_n caused by the difference in the cell dimensions and the ω_0 correction to eliminate any errors in the absolute scaling. The least-squares results are given in Table 1 for measurements at both 50 and 230 Hz and are broken down into components A and B with reference to the polarity of the external field (see Fig. 2). It should be noted that the 230 Hz values refer to a smaller effective field because of the RC rise-time voltage reduction caused by the limited current output of the power supplies. The least-squares agreement values R are defined as

$$R = \sum |I_{calc} - I_{obs}| / \sum |I_{obs}|. \quad (4)$$

Selected crystal data from Abrahams & Marsh (1986) are given in Table 2.

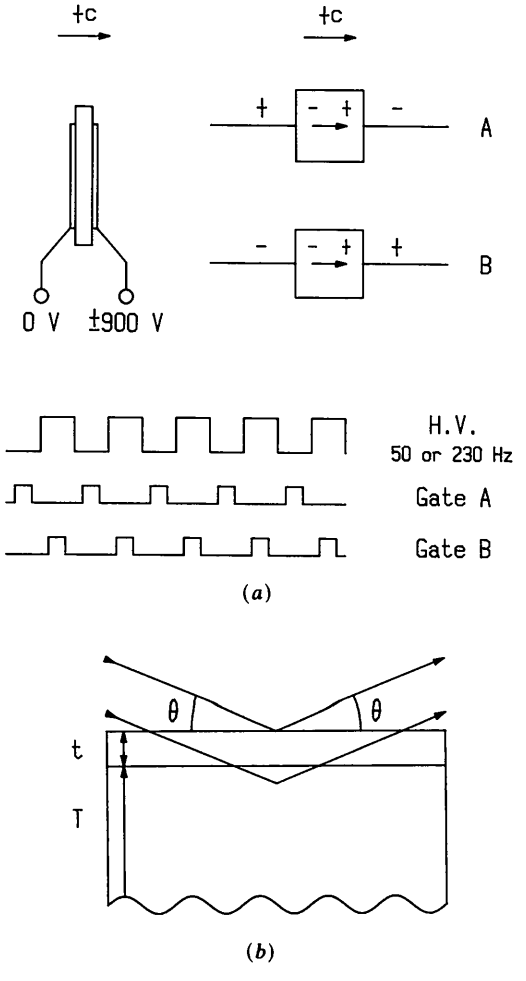

Fig. 2. (*a*) Crystal and electric field polarity. (*b*) Diffraction geometry.

Intensity evaluation

Analysis of the integrated intensities is dependent on the scattering formalism used. Complete expressions for the different cases are given in the Appendix. The diffraction geometry is illustrated in Fig. 2(*b*). The data were collected in a bisecting mode that effectively reduces the direction cosines for the incoming and diffracted beams to sin θ. The minor differences in structure factors and diffraction angles for the two phases were disregarded in the following analysis.

In the case of two layers of ideally imperfect crystal, the ratio between the intensity of the surface layer and the total observed intensity, for a given reflection, can be expressed as:

$$\xi = I^t/I^{tot} = I^t/(I^t + I^T) = 1 - \exp(-2\mu t/\sin\theta) \quad (5)$$

assuming the thickness T of the stoichiometric phase to be large [*i.e.* $\exp(-2\mu T/\sin\theta)$ is small]. The normal absorption (μ) factor was determined experimentally to be 132·5 cm^{-1}; the intensity contribution from the back surface is thus negligible [$<\exp(-0\cdot04\times132\cdot5) = 5\times10^{-3}$].

In the case of an ideally perfect crystal where both layers are sufficiently thick, the ratio can be expressed as a series:

$$\xi = [1+\exp(-2\mu t/\sin\theta)]^{-1} = 1 - \exp(-2\mu t/\sin\theta) + \exp(-4\mu t/\sin\theta) + \ldots \simeq 1 - \exp(-2\mu t/\sin\theta). \quad (6)$$

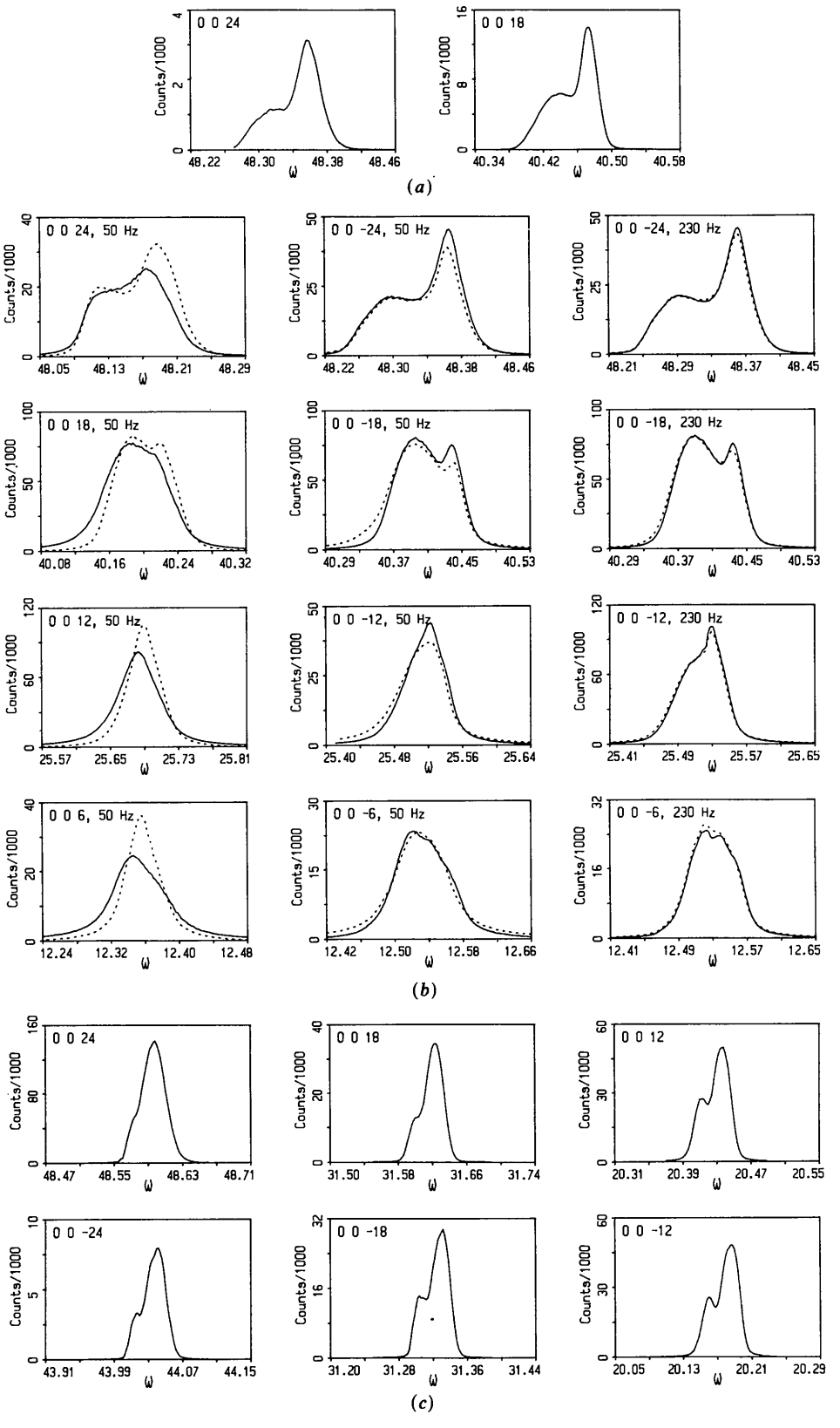

Fig. 3. (*a*) 00*l* reflections collected before the electric field was applied. $\lambda = 0{\cdot}989$ Å. (*b*) 00*l* diffraction profiles under applied ±900 V electric fields at 50 and 230 Hz. Full line denotes *A*-type field and broken lines denote *B*-type field (see Fig. 2). (*c*) 00*l* reflections collected from outside the Al layer. $\lambda = 0{\cdot}807$ Å.

Table 1. *Least-squares parameters from the Gaussian profile fit for stoichiometric* $LiNbO_3$

h k l		I_N	I_S	σ_N	σ_S	$\Delta\omega$	R
1. $f=50$ Hz							
0 0 24	A*	1644 (12)	3178 (14)	0·0204 (1)	0·0260 (1)	0·0565 (2)	0·037
	B*	1913 (15)	3790 (17)	0·0193 (2)	0·0257 (1)	0·0537 (1)	0·034
0 0 18	A	6229 (68)	7390 (76)	0·0264 (3)	0·0272 (3)	0·0394 (5)	0·071
	B	7526 (30)	5782 (31)	0·0197 (1)	0·0179 (1)	0·0417 (1)	0·034
0 0 −24	A	3548 (34)	3431 (27)	0·0314 (3)	0·0172 (1)	0·0652 (3)	0·062
	B	3532 (32)	2693 (25)	0·0329 (3)	0·0165 (1)	0·0623 (3)	0·066
0 0 −18	A	9979 (51)	3746 (43)	0·0244 (1)	0·0132 (1)	0·0462 (2)	0·056
	B	12031 (51)	1487 (32)	0·0319 (1)	0·0095 (2)	0·0457 (2)	0·050
0 0 −12	A	4211 (22)	791 (19)	0·0265 (1)	0·0119 (2)	0·0121 (4)	0·060
	B	4161 (32)	743 (26)	0·0294 (2)	0·0122 (4)	0·0165 (6)	0·081
2. $f=230$ Hz							
0 0 24	A	3548 (34)	16373 (44)	0·0134 (1)	0·0257 (1)	0·0515 (1)	0·030
	B	4011 (42)	16508 (54)	0·0135 (1)	0·0252 (1)	0·0537 (1)	0·034
0 0 18	A	6535 (37)	6773 (41)	0·0187 (1)	0·0207 (1)	0·0405 (2)	0·044
	B	6088 (31)	6882 (35)	0·0168 (1)	0·0198 (1)	0·0401 (1)	0·036
0 0 −24	A	3296 (34)	3265 (26)	0·0300 (3)	0·0160 (1)	0·0642 (2)	0·066
	B	3311 (35)	3088 (28)	0·0303 (3)	0·0162 (1)	0·0631 (3)	0·070
0 0 −18	A	9668 (49)	3715 (40)	0·0232 (1)	0·0125 (1)	0·0461 (2)	0·053
	B	9939 (44)	3578 (37)	0·0242 (1)	0·0133 (1)	0·0466 (2)	0·051
0 0 −12	A	9757 (49)	1718 (35)	0·0265 (1)	0·0091 (2)	0·0190 (3)	0·058
	B	9871 (46)	1593 (32)	0·0272 (1)	0·0088 (2)	0·0205 (3)	0·059
0 0 −6	A	3157 (15)	225 (11)	0·0252 (1)	0·0090 (4)	0·0306 (3)	0·053
	B	3366 (15)	143 (10)	0·0256 (1)	0·0076 (4)	0·0290 (3)	0·057
3. Profiles under Al electrodes before the electric field was turned on							
0 0 24		114 (1)	202 (1)	0·0203 (2)	0·0127 (1)	0·0455 (1)	0·047
0 0 18		695 (3)	592 (2)	0·0214 (1)	0·0094 (1)	0·0378 (1)	0·033
0 0 −24		161 (2)	239 (2)	0·0256 (3)	0·0173 (1)	0·0534 (2)	0·070
0 0 −18		440 (8)	788 (7)	0·0167 (3)	0·0147 (1)	0·0388 (2)	0·066
4. Profiles outside Al electrodes ($\lambda=0{\cdot}807$ Å); no electric field							
0 0 24		700 (14)	9358 (21)	0·0057 (1)	0·0132 (1)	0·0263 (1)	0·016
0 0 18		374 (13)	1723 (15)	0·0064 (2)	0·0094 (1)	0·0245 (2)	0·057
0 0 12		993 (26)	2474 (29)	0·0073 (2)	0·0093 (1)	0·0257 (2)	0·070
0 0 −24		75 (6)	442 (8)	0·0051 (3)	0·0106 (2)	0·0253 (4)	0·102
0 0 −18		470 (22)	1467 (26)	0·0065 (3)	0·0094 (2)	0·0253 (3)	0·108
0 0 −12		878 (30)	2477 (35)	0·0069 (2)	0·0094 (3)	0·0264 (3)	0·090

* *A* and *B* refer to the polarity of the external field, *cf.* Fig. 2(*a*).

For a very thin (≤ 1 μm) ideally perfect surface layer, the scattering approaches that of an ideally imperfect crystal and the intensity contributions are no longer directly comparable. The two contributions can be placed on a common scale by means of the expression

$$\Gamma = I^{\text{ideally imperfect}}/I^{\text{ideally perfect}}$$
$$= [1-\exp(-2\mu x/\sin\theta)]\pi(1+k^2)/4|g|R^y, \quad (7)$$

where g and R^y are given in the Appendix. For $x = T$, the exponential factor vanishes and

$$\xi_\Gamma = I^t/(I^t+\Gamma I^T) = 1-\exp(-2\mu t_\Gamma/\sin\theta). \quad (8)$$

The thickness of each surface layer (t) was calculated for the two models using the observed intensities $I_n = I^t$ and $I_s = I^T$ and (5) and (8). The results are listed in Table 3.

Discussion

Fig. 3 illustrates the reflection profiles recorded from the area under the Al electrodes before and after an electric field was applied. For comparison six profiles from an area outside the Al electrodes recorded at the conclusion of the experiment without a field are also shown.

Table 2. *Crystal data for stoichiometric* (S) *and congruent* (C) $LiNbO_3$

Space group $R3c$, $Z=6$, $\lambda=0{\cdot}989$ Å.

Composition 1	(S) $LiNbO_3$	(C) $Li_{0{\cdot}941}Nb_{1{\cdot}012}O_3$	
a (Å)*	5·1474 (1)	5·1506 (1)	
c (Å)*	13·8561 (1)	13·86496 (3)	
μ (mm^{-1})	13·2	13·3	
			$\Delta\theta$
θ_{006}(°)	12·3645	12·3564	0·0081
θ_{0012}(°)	25·3571	25·3398	0·0173
θ_{0018}(°)	39·9702	39·9395	0·0307
θ_{0024}(°)	58·9279	58·8671	0·0608

* Abrahams & Marsh (1986).

Inspection of Fig. 3 shows that all profiles taken from below the Al electrodes give evidence of peak splitting, indicating the existence of surface layers of different d spacing. Before electric-field treatment, the surface-layer thickness is about 0·015 mm thick, using (5) for the calculations and 0·007 mm if (8) is used. The values for Gaussian spread parameters (*cf.* σ_N, σ_S in Table 1) are twice as large for (00.l) surface

Table 3. *Calculated thickness of modified layer on stoichiometric* $LiNbO_3$

Values of Γ (equation 7): 00.24 2·105; 00.18 3·133; 00.12 4·582; 00.6 4·532 ($\mu = 132{\cdot}5\ cm^{-1}$). The value of 00.18 with field *B* and frequency 50 Hz was not used in calculation of average surface thickness.

h k l		ξ	ξ_Γ	*t* (mm)	t_Γ (mm)
1. $f = 50$ Hz					
0 0 24	*A*	0·3409 (28)	0·1973 (16)	0·0135 (2)	0·0071 (2)
	B	0·3354 (29)	0·1934 (17)	0·0132 (2)	0·0069 (2)
0 0 18	*A*	0·4575 (61)	0·2120 (29)	0·0148 (3)	0·0058 (3)
	B	0·5655 (29)	0·2935 (17)	0·0202 (2)	0·0084 (2)
0 0 −24	*A*	0·5084 (58)	0·3294 (38)	0·0229 (3)	0·0129 (3)
	B	0·5674 (63)	0·3839 (43)	0·0271 (4)	0·0156 (4)
0 0 −18	*A*	0·7271 (51)	0·4595 (38)	0·0315 (3)	0·0149 (3)
	B	0·8900 (55)	0·7209 (57)	0·0535 (5)	0·0309 (5)
0 0 −12	*A*	0·8419 (66)	0·5374 (68)	0·0298 (4)	0·0125 (4)
	B	0·8485 (97)	0·5499 (99)	0·0305 (6)	0·0129 (6)
2. $f = 230$ Hz					
0 0 24	*A*	0·1781 (18)	0·0933 (9)	0·0063 (1)	0·0032 (1)
	B	0·1955 (21)	0·1035 (11)	0·0070 (2)	0·0035 (1)
0 0 18	*A*	0·4911 (34)	0·2355 (18)	0·0164 (2)	0·0065 (1)
	B	0·4694 (29)	0·2202 (14)	0·0154 (2)	0·0060 (2)
0 0 −24	*A*	0·5024 (61)	0·3241 (39)	0·0226 (3)	0·0127 (3)
	B	0·5174 (66)	0·3375 (43)	0·0235 (4)	0·0133 (4)
0 0 −18	*A*	0·7724 (50)	0·4537 (37)	0·0311 (3)	0·0147 (3)
	B	0·7353 (45)	0·4700 (35)	0·0322 (3)	0·0154 (3)
0 0 −12	*A*	0·8503 (62)	0·5535 (60)	0·0307 (3)	0·0130 (4)
	B	0·8610 (58)	0·5748 (58)	0·0319 (3)	0·0318 (4)
0 0 −6	*A*	0·9335 (68)	0·7559 (101)	0·0219 (4)	0·0114 (4)
	B	0·9592 (65)	0·8385 (106)	0·0258 (6)	0·0147 (6)
3. Below Al electrodes, before field was applied					
0 0 24		0·361 (4)	0·211 (2)	0·0145 (2)	0·0077 (2)
0 0 18		0·540 (3)	0·273 (1)	0·0188 (1)	0·0077 (1)
0 0 −24		0·402 (6)	0·242 (4)	0·0166 (4)	0·0090 (4)
0 0 −18		0·358 (7)	0·151 (3)	0·0107 (3)	0·0040 (3)
4. Away from Al electrodes, no field applied; $\lambda = 0{\cdot}807$ Å, Γ (equation 7): 00.24 2·161; 00.18 4·553; 00.12 6·377; $\mu = 74{\cdot}5\ cm^{-1}$					
0 0 24		0·070 (1)	0·033 (1)	0·0034 (2)	0·016 (1)
0 0 18		0·178 (6)	0·046 (2)	0·0069 (5)	0·0016 (4)
0 0 12		0·286 (8)	0·059 (2)	0·0079 (4)	0·0014 (4)
0 0 −24		0·145 (12)	0·073 (6)	0·0073 (12)	0·0035 (12)
0 0 −18		0·243 (12)	0·066 (3)	0·0098 (9)	0·0024 (9)
0 0 −12		0·262 (10)	0·053 (2)	0·0071 (5)	0·0013 (5)

layers denoted *N* as for the bulk stoichiometric phase denoted *S*. A tendency for surface-layer formation in the area outside the Al electrodes is also detected but here they appear to be much thinner (0·007 or 0·002 mm, respectively).

The profiles below the Al surface change markedly under an applied electric field. The most obvious effect is the broadening of the Gaussian spread associated with the stoichiometric phase on the +**c** side (see Table 1) where the σ_S increases from an average of 0·01 to 0·024. The averages on the −**c** side are virtually identical, 0·016 and 0·013, before and after field application.

Calculations using (5) or (8) give a difference in the apparent thickness of the (00.1) and (00.$\bar{1}$) surface layers. Equation (8), for instance, gives an average (00.$\bar{1}$) thickness of 0·0138 (12) mm compared to 0·0059 (18) mm for (00.1). It is, however, not clear if this apparent change caused by the electric field is an actual change in surface-layer thickness or if it is a computational artefact caused by the assumption of equal-scattering theory for the two sides. This assumption may not be correct since the Gaussian spread parameters change differently for the two sides. Further studies must be made to ascertain definitively if the results are indeed related to a structure dependency or are due only to a reduction in crystal perfection for the stoichiometric phase on the +**c** side of the crystal.

The resolution provided by the synchrotron radiation, however, allows the nature of the surface layer to be investigated further. Differentiation of Bragg's law yields

$$\Delta d/d = -\cot\theta\,\Delta\theta. \qquad (9)$$

Hence it is possible to calculate $\Delta c/c$ from the separation observed between Bragg diffraction profiles. The highest-resolution data (*i.e.* 00.24) give an average value of $6{\cdot}2\times10^{-4}$ for $\Delta c/c$. The values for the two field frequencies show no deviations but there is a small systematic difference of $\pm0{\cdot}5\times10^{-4}$ between the positive and negative directions along the *c* axis, probably indicating the level of accuracy in our measurements. The $\Delta c/c$ values calculated for lower-order 00.*l* show a broader range from 4·5 to $9{\cdot}7\times10^{-4}$. It is interesting to compare this values with that expected from a mixture of stoichiometric and congruent $LiNbO_3$ using the high-precision unit-cell

dimensions in Table 2. This calculation gives $\Delta c/c = 6{\cdot}4\times10^{-4}$, which is an excellent agreement with the observation suggesting that the new phase may be a congruent-composition surface layer. Contemplation of the nature of the surface layer, however, indicates that at least two hypotheses are possible. The first takes the near identity of the *c*-axis length and that of congruent lithium niobate as an indication of identity of composition. The second assumes that Al atoms from the evaporated electrodes have in-diffused to the $LiNbO_3$ plate. Both hypotheses may be examined.

A change in composition from stoichiometric to congruent at room temperature is possible although many studies on stoichiometric $LiNbO_3$ plates under lower applied electric fields (on the order of 100 V) have given no evidence for composition changes at room temperature. A frequency dependence of dielectric properties has, however, been reported (Watson, 1986).

In the second hypothesis, Al atoms are considered to diffuse into stoichiometric $LiNbO_3$ and partially replaced Li; the ionic radii of Al^{3+} and Ti^{4+} are comparable [0·54 and 0·61 Å, respectively; Shannon (1976)], and in-diffusion of the slightly larger Ti^{4+} is readily achieved in producing waveguides on $LiNbO_3$. Ti^{4+} in-diffusion is achieved over a period of days at temperatures around 1270 K and the concentration profiles obtained show penetration depths to about 4 μm (Aksenov, Kukharev, Lipovskaya, Lipovskii & Pavlenko, 1987). The in-diffusion of titanium has been proposed to proceed *via* a rutile solid-solution phase, *i.e.* $LiNb_3O_8$–TiO_2 (Rice & Holmes, 1986). The diffusion constant of Al^{3+} ions is very small, even at elevated temperatures, with a value of $D = 10^{-14}$ m^2 s^{-1} at 2200 K for Al^{3+} in Al_2O_3 (Paladino & Kingery, 1962).

Further work is clearly needed to obtain detailed information on the surface layer formed in the present experiment. A test of the above hypotheses is not readily undertaken by examination of the surface layers *in vacuo* by electron spectroscopy methods because of the limited penetration depth (less than 50 Å) or, in the case of high-energy Auger spectroscopy, because of the lack of resolution. Observations by secondary ion mass spectroscopy (SIMS) may be distorted by 'crater' formation upon Ar or Cs bombardment. Rutherford back-scattering techniques (RBS) or analytical electron microscopy (EDAX) of a cross section of the plate may yield useful information concerning the nature of the surface layer. These techniques, together with further study of the field dependence on the surface-layer formation, will be pursued in subsequent experiments.

It is a pleasure to thank Dr M. C. Nelson for valuable discussion and The Swedish Natural Science Research Council for financial support (KS).

APPENDIX

In the case of a thick ideally perfect non-centrosymmetric crystal in a narrow monochromatic beam, the integrated intensity (Weiss, 1966) for the reflecting (Bragg) mode is

$$I = \frac{I_0}{\omega}\frac{K\lambda^2 r_e|F'_H|}{\pi|b|^{0\cdot5}V\sin 2\theta}R^y$$

$$R^y = \int_{-\infty}^{\infty}\frac{1+k^2+2s}{[(1-k^2)^2+4p^2]^{0\cdot5}}[L-(L^2-1)^{0\cdot5}]\,dy$$

$$L = \frac{[(y^2-g^2+k^2-1)^2+4(gy-p)^2]^{0\cdot5}+y^2+g^2}{[(1-k^2)^2+4p^2]^{0\cdot5}},$$

where I_0 = incident-beam power; ω = angular velocity; K = polarization (for synchrotron radiation in our case, $K \simeq 1$); r_e = classical electron radius; b = ratio of direction cosines of incident and diffracted beam relative to the crystal surface, for the symmetric case, $b = -1$; V = unit-cell volume;

$$g = \frac{(1-b)\mu V}{4|b|^{0\cdot5}r_e\lambda|F'_H|K};$$

$$k = |F''_H|/|F'_H|; \quad s = -k\sin\delta; \quad p = k\cos\delta,$$

δ = difference in phase angles between real and imaginary parts of structure factor; μ = linear absorption coefficient;

$$y = [0{\cdot}5(1-b)\psi_0 + 0{\cdot}5b\alpha]/K|\psi'_H||b|^{0\cdot5},$$

where ψ_0 is the real part of the electron polarizability per unit volume (times 4π) in the forward direction and $\alpha = 2(\theta_B-\theta)\sin 2\theta_B$ where θ_B is the Bragg angle and θ is the angle the incident beam makes with the crystal planes.

In the case of a very thin ideally perfect crystal ($t \le 1$ μm) or an ideally imperfect crystal, the integrated intensity can be expressed as

$$I = \frac{I_0}{\omega}\frac{[1-\exp(-2\mu t/\sin\theta)]K^2 r_e^2\lambda^3|F_H|^2}{2\mu V^2\sin\theta},$$

t = crystal thickness, and $|F_H|^2 = |F'_H|^2 + |F''_H|^2$.

References

ABRAHAMS, S. C. (1979). *God. Jugosl. Centra Kristallogr.* **14**, 1-12.

ABRAHAMS, S. C. & MARSH, P. (1986). *Acta Cryst.* B**42**, 61-68.

AKSENOV, E. T., KUKHAREV, A. V., LIPOVSKAYA, M. YU, LIPOVSKII, A. A. & PAVLENKO, A. V. (1987). *Sov. Phys. Tech. Phys.* **32**, 84-87.

CARRUTHERS, J. R., PETERSON, G. E., GRASSO, M. & BRIDENBAUGH, P. M. (1971). *J. Appl. Phys.* **42**, 1846-1851.

COMPTON, A. H. & ALLISON, S. K. (1949). *X-rays in Theory and Experiment*, pp. 469-471. Toronto, New York, London: D. van Nostrand.

EMIS (1989). EMIS Data Review Series No. 5. *Properties of Lithium Niobate.* Institution of Electrical Engineers, London, England.

GALLAGHER, P. K. & O'BRYAN, H. M. (1985). *J. Am. Ceram. Soc.* **68**, 147-150.
KVICK, Å. (1989). Private communication.
O'BRYAN, H. M., HOLMES, R. J. & KIM, Y. S. (1984). Private communication.
PALADINO, A. E. & KINGERY, W. D. (1962). *J. Chem. Phys.* **37**, 957-962.
RÄUBER, A. (1978). *Current Topics in Materials Science*, Vol. 1, edited by E. KALDIS, pp. 481-601. Amsterdam: North-Holland.
RICE, C. E. & HOLMES, R. J. (1986). *J. Appl. Phys.* **60**, 3836-3839.
SHANNON, R. D. (1976). *Acta Cryst.* A**32**, 751-767.
WATSON, J. E. (1986). Private communication.
WEISS, R. J. (1966). *X-ray Determination of Electron Distributions.* Amsterdam: North-Holland.

Acta Cryst. (1990). A**46**, 485-489

Evaluation of Atomic Displacement Parameters by Lattice-Dynamical Calculations. Efficiency in Brillouin-Zone Sampling

BY TULLIO PILATI AND RICCARDO BIANCHI

Centro CNR per lo Studio delle Relazioni tra Struttura e Reattività Chimica, Via Golgi 19, *I*-20133 *Milano, Italy*

AND CARLO MARIA GRAMACCIOLI

Dipartimento di Scienze della Terra, Università, Via Botticelli 23, *I*-20133 *Milano, Italy*

(*Received* 3 *November* 1989; *accepted* 23 *January* 1990)

Abstract

Some progression formulae for uneven and 'asymmetric' sampling of the Brillouin zone are shown to be particularly useful to attain fast convergence in the calculation of atomic displacement parameters and thermodynamic functions by lattice-dynamical procedures.

Introduction

Lattice dynamics provides a useful way for deriving important crystal properties from structural and spectroscopic (or force-field) data. Among these properties, there are thermodynamic functions and also information about thermal behaviour (*e.g.* TDS, atomic displacement parameters or a.d.p.'s).

For instance, the atomic displacement tensor $\mathbf{U}(p)$ relative to a certain atom p can be obtained as follows:

$$\mathbf{U}(p) = (Nm_p)^{-1} \sum_{\psi,\mathbf{q}} E_\psi(\mathbf{q})[2\pi\nu_\psi(\mathbf{q})]^{-2} \times \mathbf{e}(p|\psi\mathbf{q})[\mathbf{e}^*(p|\psi\mathbf{q})]^t. \quad (1)$$

Here $\mathbf{e}(p|\psi\mathbf{q})$ is the mass-adjusted polarization vector of the atom p, $E_\psi(\mathbf{q})$ is the average energy of the mode, N is the total number of unit cells in the crystal and m_p is the mass of the atom (see, for instance, Willis & Pryor, 1975).

Similarly, thermodynamic functions such as the molar heat c_v and entropy S can be derived from the same data:

$$c_v = 3R \sum_\nu g_\nu (h\nu/kT)^2 \exp(h\nu/kT) \times [\exp(h\nu/kT) - 1]^{-2} \Delta\nu \quad (2)$$

$$S = E_{\text{vib}}/T - 3R \sum_\nu g_\nu \ln[1 - \exp(h\nu/kT)]\Delta\nu, \quad (3)$$

where E_{vib} is the vibrational energy of the crystal and g_ν is a density-of-states function, normalized so that $\sum_\nu g_\nu \Delta\nu = 1$. The summations are extended to all the vibrational modes (ψ) of frequency ν_ψ for a certain point of the Brillouin zone corresponding to a certain value of the wave vector $\mathbf{q}$ and (in principle) to all the values of $\mathbf{q}$ in the Brillouin zone.

The necessity of sampling the Brillouin zone at a sufficient number of points is one of the major practical difficulties. For some thermodynamic functions, considerable efforts have already been made to define an efficient way to obtain an accurate description of the density of states of a material from a limited sampling (see, for instance, Baldereschi, 1972; Chadi & Cohen, 1973; Price, Parker & Leslie, 1987). The situation becomes considerably more critical if a.d.p.'s or their molecular counterparts [such as **T**, **L** and **S** in Schomaker-Trueblood's (1968) notation]

0108-7673/90/060485-05$03.00